

Supporting Information

Amorphous anion skeletons induced rapid and cation-selective ion flux towards stable aqueous zinc-iodine batteries

Zhenjing Jiang^[a,b], Zijuan Du^[c], Kailin Luo^a, Yanfei Zhang^[d], Hang Yang^[b], Wei Zhang^[b], Ruwei Chen^[b], Jie Chen^[b], Zhe Cui^[b], Fuhan Cui^[a], Rui Pan^[a], Guoju Zhang^[a], Shuangying Lei^[a], Litao Sun^[a], Kuibo Yin^[a,*], Guanjie He^[b,*]

^a *SEU-FEI Nano-Pico Center, Key Laboratory of MEMS of Ministry of Education, Southeast University, Nanjing 210096, China.*

^b *Christopher Ingold Laboratory, Department of Chemistry, University College London, London WC1H 0AJ, UK.*

^c *State Key Laboratory of Silicate Materials for Architectures, Wuhan University of Technology, Wuhan 430070, P.R. China*

^d *School of Materials Science and Engineering, Qilu University of Technology, Jinan 250353, China.*

*Corresponding authors. E-mails: yinkuibo@seu.edu.cn; g.he@ucl.ac.uk

Experiment section

Synthesis of the crystalline and amorphous $\text{Na}_2\text{Zn}_2(\text{TeO}_3)_3$: The crystalline $\text{Na}_2\text{Zn}_2(\text{TeO}_3)_3$ was prepared through a facial solvothermal method. In detail, the $\text{ZnSO}_4 \cdot 7\text{H}_2\text{O}$ and Na_2TeO_3 were dissolved in the deionized water with a molar ratio of 2: 3. Then the solution was transferred to a reactor and heated for 10 h in the oven at 100 °C. Washed the products several times with Ethanol and deionized water, the $\text{Na}_2\text{Zn}_2(\text{TeO}_3)_3$ sample was acquired after drying them in the vacuum oven overnight. The amorphous one was prepared by heating the crystalline $\text{Na}_2\text{Zn}_2(\text{TeO}_3)_3$ at 180 °C for 2 h in the Ar atmosphere.

Preparation of Zn anodes: The Zn anodes with crystalline and amorphous $\text{Na}_2\text{Zn}_2(\text{TeO}_3)_3$ artificial layer were prepared through the doctor blade method. Specifically, the surface of commercial Zn (purity: 99.999%; thickness: 50 μm) were sanded using sandpapers with a grit size of 1,000 to eliminate the oxide layer and then cleaned by the ethanol. The crystalline and amorphous $\text{Na}_2\text{Zn}_2(\text{TeO}_3)_3$ powders (90 wt%), polyvinylidene difluoride (10 wt%), and the N-Methyl-2-pyrrolidone were mixed to acquire the slurries. Subsequently, the acquired slurries were coated on the clean Zn foils and noted as CNZT@Zn and ANZT@Zn, respectively, and the commercial Zn foil is named bare Zn.

preparation of MnO_2 , $\text{NH}_4\text{V}_4\text{O}_{10}$, and iodine cathodes: The MnO_2 was synthesized through a solvothermal method based on previous literature.^[1] In detail, $\text{MnSO}_4 \cdot \text{H}_2\text{O}$ (0.4566 g) and H_2SO_4 (1.5 mL, 1 M) were dissolved in 70 mL of deionized water. The KMnO_4 (15 mL, 0.2 M) solution was added to the above solution. Then, the solution was transferred into an oven and heated at 200 °C for 20 h. After cooling to room temperature, the product was washed with deionized water several times and dried at 60 °C for 18 h. The $\text{NH}_4\text{V}_4\text{O}_{10}$ was also prepared using the hydrothermal method.^[2] Dissolving 3 mmol NH_4VO_3 into 40 ml deionized water, and then add 4.8 mmol $\text{H}_2\text{C}_2\text{O}_4 \cdot 2\text{H}_2\text{O}$. Subsequently, the above solution was transferred into a 50 mL Teflon-lined stainless autoclave and heated at 160 °C for 6 h. After cooling naturally to room temperature, the product was washed with distilled water several times and dried at 80

°C for 10 h. The mixture of active carbon and iodine powder (in a mass ratio of 1: 1) was mixed in a sealed Teflon-liner and then heated at 100 °C for 6 h to acquire the cathode material. The MnO₂/NH₄V₄O₁₀/iodine cathodes were prepared by mixing cathode material (70 wt%), conductive acetylene black (20 wt%), and polyvinylidene fluoride (10 wt%). The mixture was coated on carbon paper, dried in the oven at 60 °C for 10 h and then cut into circular electrode slices.

Simulation Method: All the first-principles calculations were performed with the VASP package, and the projector augmented wave (PAW) method was adopted to incorporate core electrons into pseudopotentials. Moreover, the exchange-correlation functional parametrized by Perdew-Burke-Ernzerhof (PBE) was employed. The electronic Brillouin zone and plane-wave cutoff energy were set at 500 eV. The Gamma scheme k-mesh of $2 \times 4 \times 1$ was utilized for the convergence of total energy with a criterion of 1×10^{-5} eV per atom, and the residual force on each atom was 3 less than $0.03 \text{ eV } \text{Å}^{-1}$. To model O site and Te site of Na₂Zn₂(TeO₃)₃ crystal and the Zn (002) facet with Zn atom adsorbed, a 15 Å vacuum was added into the z-direction. The binding energy E_b could be calculated through $E_b = E_{\text{total}} - E_{\text{slab}} - E_{\text{Zn}}$, where the E_{total} , E_{slab} , and E_{Zn} represented the total energy of O site and Te site of Na₂Zn₂(TeO₃)₃ crystal and the Zn (002) facet with Zn atom, the energy without Zn atom, and the energy of the Zn atom, respectively.

The MD simulation is performed using CP2k software. As a starting point, the unit cell structure of crystalline Na₂Zn₂(TeO₃)₃ was replicated into a $1 \times 1 \times 3$ supercell (202 atoms, the hydrogen atoms are omitted) for better statistical averaging of structures. Initially, structure optimization for the constructed supercell was performed to acquire the structure model of amorphous Na₂Zn₂(TeO₃)₃. The structure model was then heated to 453 K at a rate of 86.6 K ps^{-1} and kept for 5 ps. Afterwards, the structure was cooled to 300 K at a rate of 86.6 K ps^{-1} before equilibration for another 5 ps.

Materials characterization

X-ray diffraction (XRD, Bruker D2 Phase) measurements of the powders samples and electrodes were performed with Cu K α ($\lambda=1.5406 \text{ Å}$). The scanning electron

microscopy (SEM, Dualbeam Helios 5CX) measurements were used to acquire the Zn deposition morphology on those Zn anodes. Besides, the 2 M ZnSO₄ electrolyte was used to measure the static contact angle on different anodes (JY-82B Kruss DSA). The Inductively Coupled Plasma (ICP) measurement is conducted with ICP-OES: Agilent 5110 (U.S.A), and the final result is the average of the three measurement values. The in-situ Raman spectroscopy measurements were conducted via In-Via Raman microscopic with an Ar⁺ laser ($\lambda = 600$ nm) at 50 \times aperture. The X-ray photoelectron spectroscopy (XPS) measurements were carried out with a Thermo Scientific K-Alpha. Transmission electron microscopy (TEM) images were acquired using an image aberration-corrected FEI Titan microscope at 300 kV.

Fabrication of Batteries and Electrochemical Measurement

The electrochemical performance of the bare Zn, CNZT@Zn, and ANZT@Zn anodes was evaluated by assembling the coin-type cell CR2025. For the symmetric cell, the Zn anode was cut into round pieces, and the electrolyte was composed of 2 M ZnSO₄ aqueous solution. For the Zn||Cu half cells, bare Cu, CNZT@Cu, and ANZT@Cu were used as the working electrode and Zn foil was used as the counter electrode. The full cell was assembled by one of the three Zn anodes and MnO₂ cathode (with 2 M ZnSO₄ + 0.2 M MnSO₄ electrolyte), or NH₄V₄O₁₀ cathode (with 2 M Zn(CF₃SO₃)₂ electrolyte), or iodine cathode (with 2 M ZnSO₄ electrolyte). The galvanostatic charge/discharge tests of cells were carried out on a Land instrument. The cyclic voltammetry curves over the range of 1.0–1.85 V for full cells (–0.2 to 0.8 V for half cells) and the EIS test in a frequency range of 10^{–2} to 10⁶ Hz were recorded with the CHI760 electrochemical workstation. The Tafel plot for symmetric cells was tested in a voltage range from –200 to 200 mV (vs. Zn/Zn²⁺) at a scan rate of 1 mV s^{–1}. The Zn||C coin type cells were used to record the LSV curves with a scan rate of 10 mV s^{–1}. The Chronoamperometry (CA) measurement was conducted on symmetric cells by applying a constant overpotential of –150 mV for 250 s. Besides, the Zn coulombic efficiency was measured in Zn||Cu half-cells. in detail, a fixed amount of Zn (0.5 mAh cm^{–2}) was plated on the Cu electrode and then stripped back until the cutoff voltage arrived at 0.6 V.

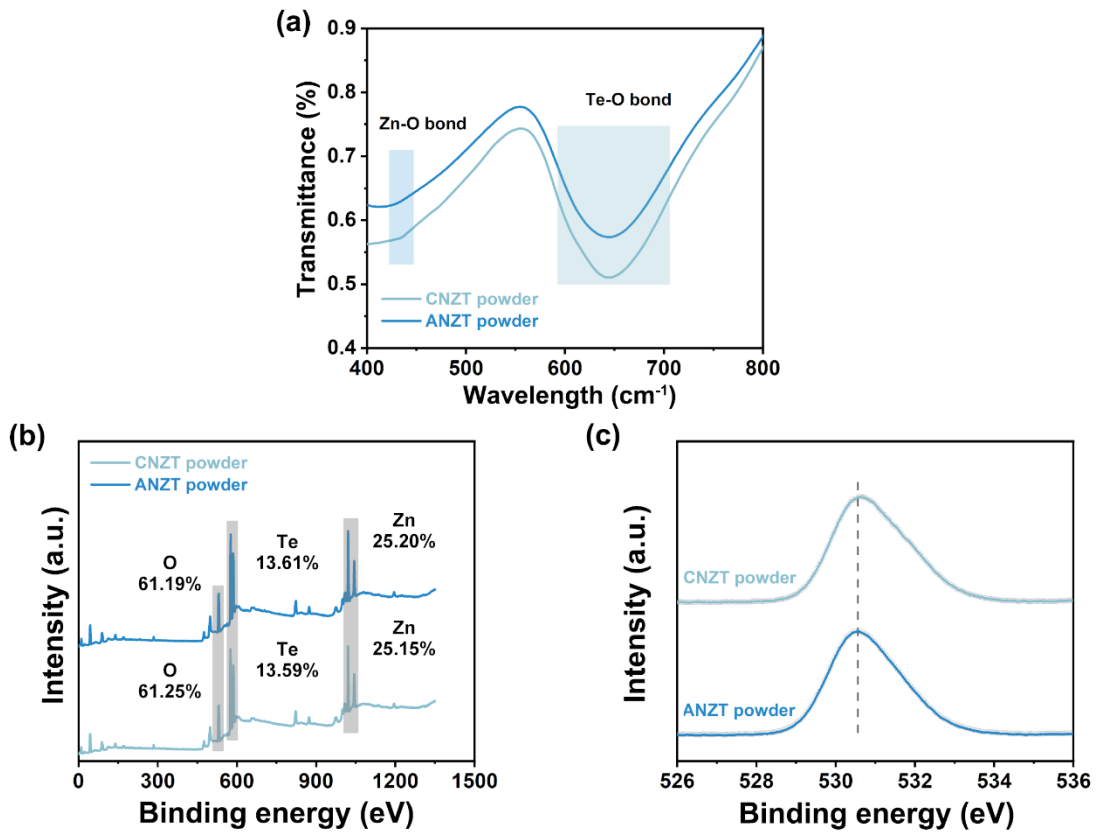


Fig. S1 (a) FTIR spectra of CNZT and ANZT powders. (b) XPS survey spectra of CNZT and ANZT powders. (c) High-resolution XPS spectra of O 1s of CNZT and ANZT powders.

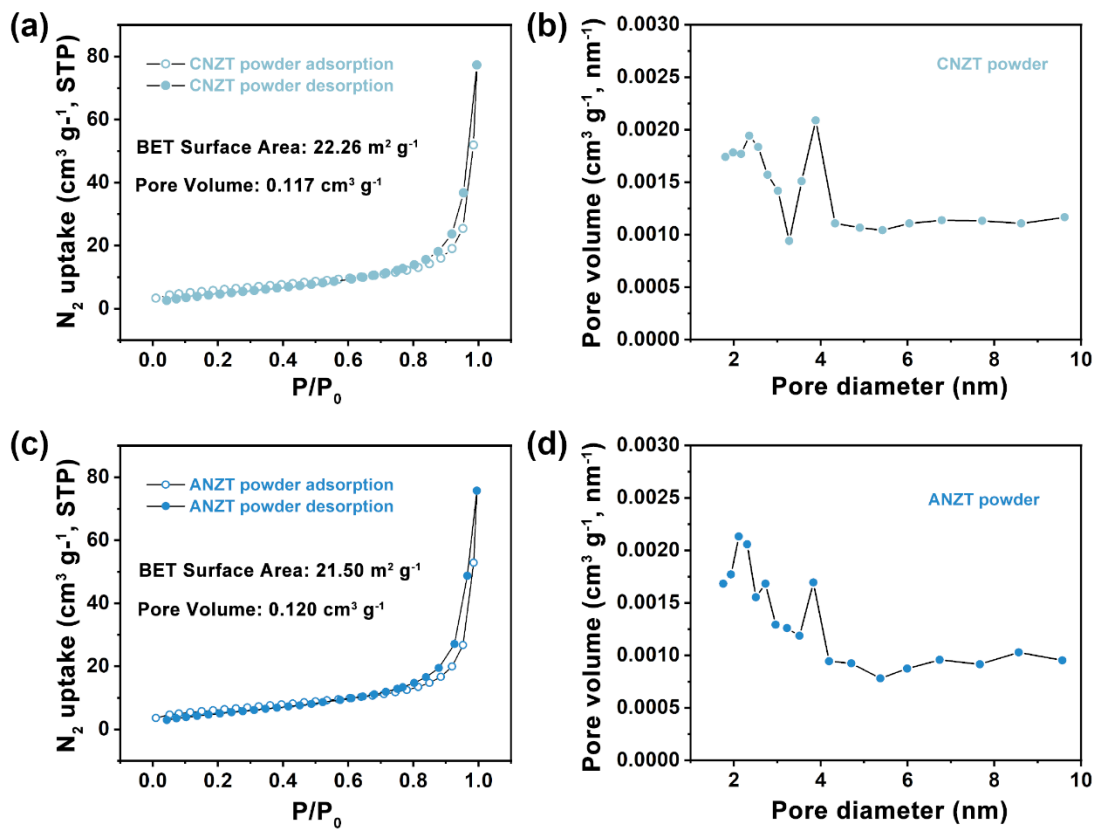


Fig. S2 (a,c) The N_2 adsorption/desorption isothermal curves and (b,d) pore size distribution of CNZT and ANZT powders.

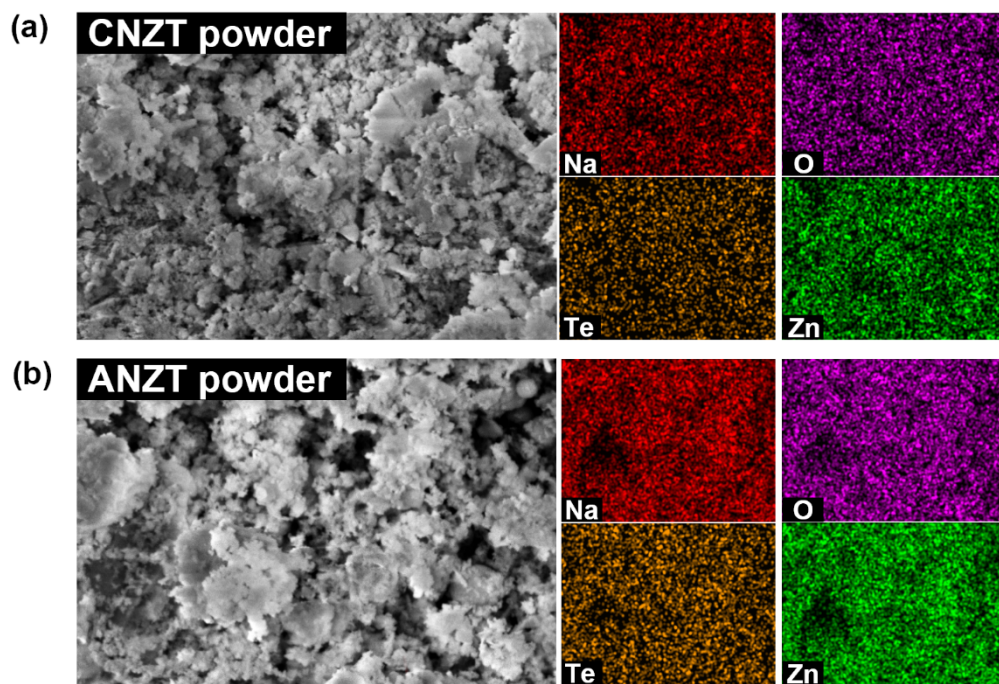


Fig. S3 The SEM images of CNZT and ANZT powders with corresponding EDS mapping results.

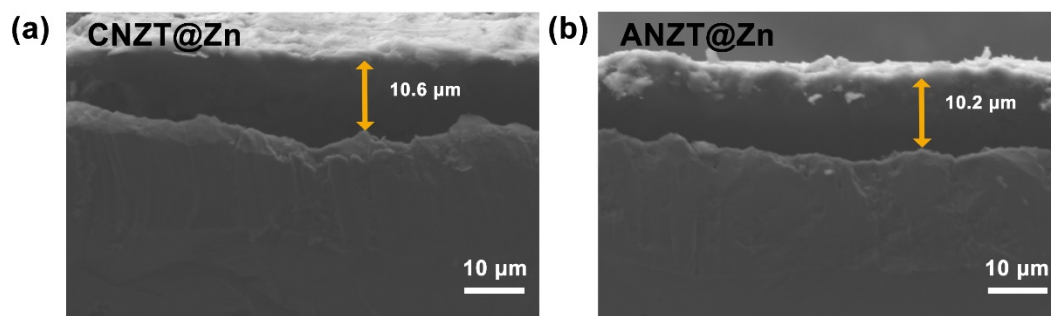


Fig. S4 The side-view SEM images of CNZT@Zn and ANZT@Zn anodes, the thickness of prepared interlayers is marked.

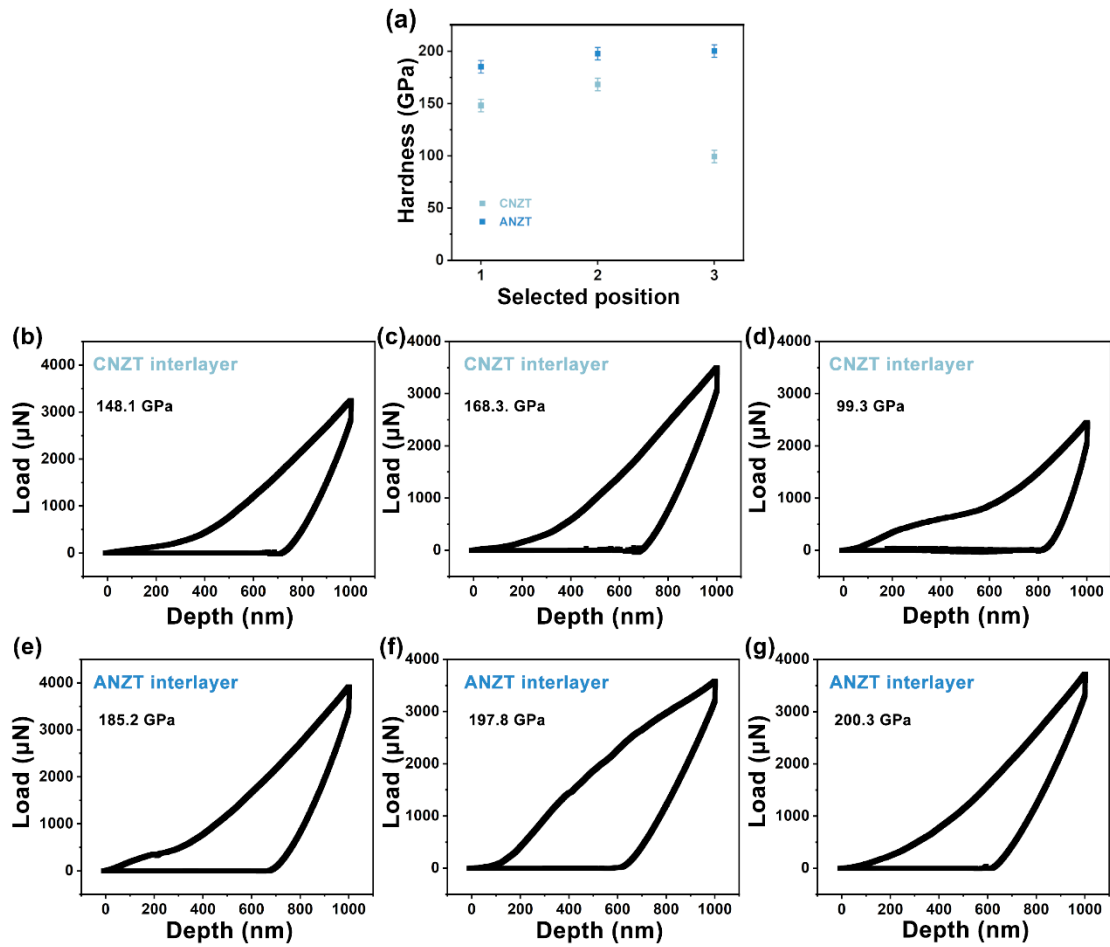


Fig. S5 The calculated hardnesses of CNZT and ANZT interlayers that based on the nanoindentation measurements (the indentation depth is fixed at 500 nm). (b-g) The test force vs. indentation depth curves of nanoindentation measurement on the CNZT and ANZT interlayers.

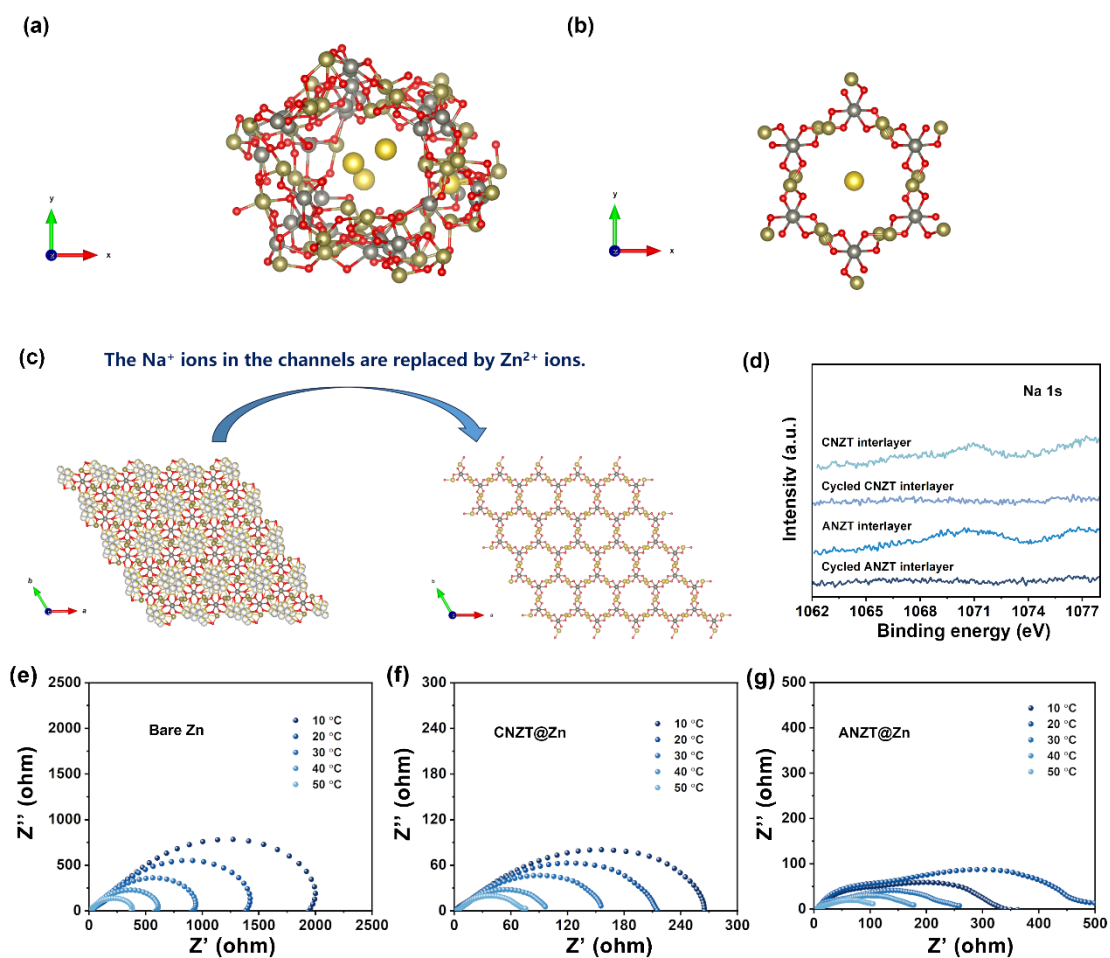


Fig. S6 (a,b) The structure model of ANZT (after MD simulation) and CNZT samples. (c) The schematic diagram of the formation of $\text{Zn}_2(\text{TeO}_3)^{2-}$ anion channel during the Zn deposition process. (d) High-resolution Na 1s XPS spectra of CNZT and ANZT interlayers before and after 20 cycles at $5 \text{ mA cm}^{-2}/5 \text{ mAh cm}^{-2}$. (e-g) Temperature-varied (10 °C, 20 °C, 30 °C, 40 °C, and 50 °C) Nyquist plots of symmetric cells with bare Zn, CNZT@Zn, and ANZT@Zn anodes.

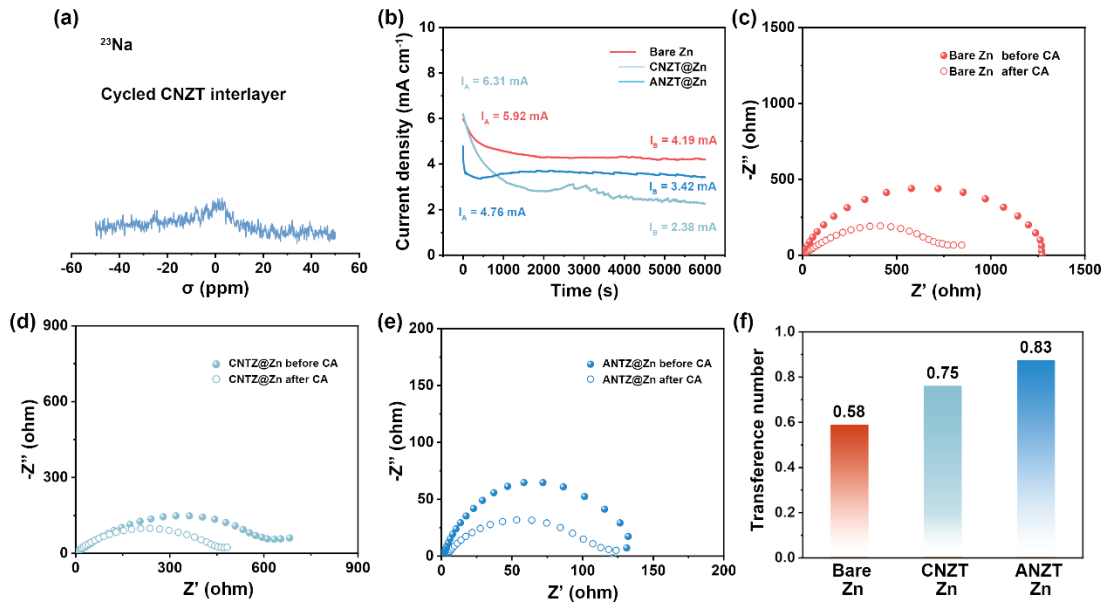


Fig. S7 (a) ^{23}Na NMR spectrum of cycled CNZT interlayer (after 1 cycle at $5 \text{ mA cm}^{-2}/2.5 \text{ mAh cm}^{-2}$). (b) CA curves of bare Zn, CNZT@Zn, and ANZT@Zn anodes under an overpotential of -25 mV . The Nyquist plots of symmetric cells with (c) bare Zn, (d) CNZT@Zn, and (e) ANZT@Zn anodes. (f) The calculated ion transference number of bare Zn, CNZT@Zn, and ANZT@Zn anodes.

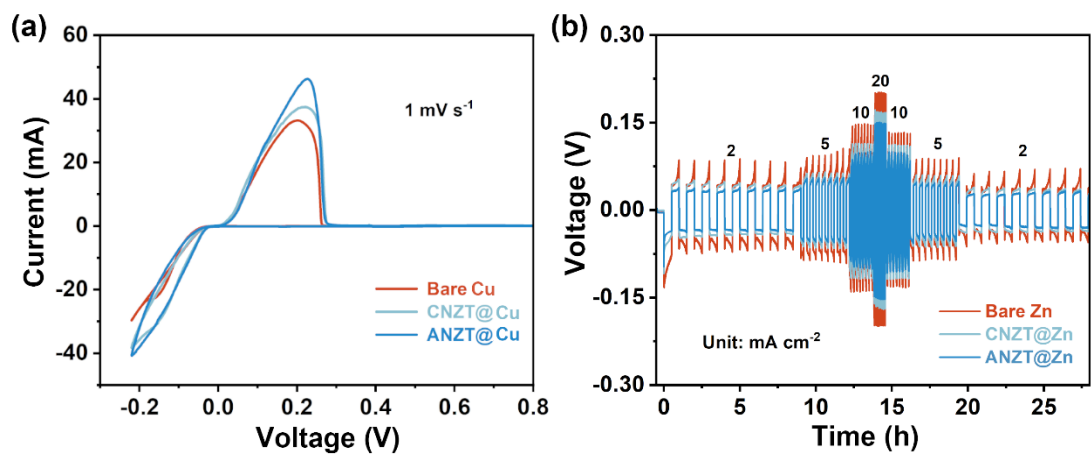


Fig. S8 (a) CV curves of Zn||Cu half-cells with bare Cu, CNZT@Cu, and ANZT@Cu electrodes. (b) Rate performance of symmetric cells with bare Zn, CNZT@Zn, and ANZT@Zn anodes.

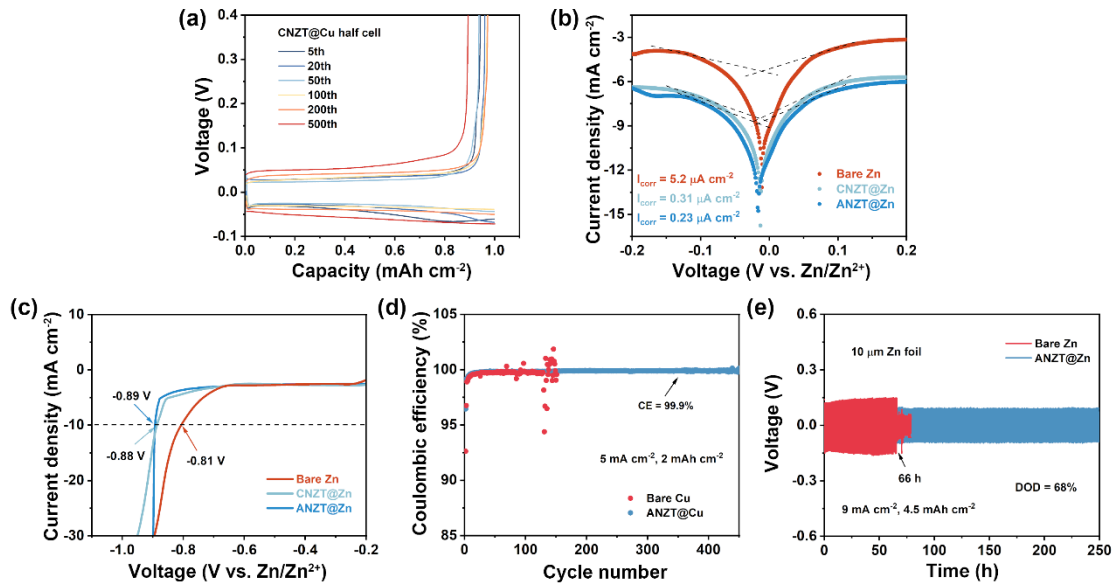


Fig. S9 (a) Charge/discharge curves of Zn||CNZT@Cu half-cell at different cycle numbers (1 mA cm⁻²/1 mAh cm⁻²). (b) Tafel and (c) LSV curves of bare Zn, CNZT@Zn, and ANZT@Zn anodes. (d) The CE test of Zn||Cu half-cells with bare Cu and ANZT@Cu electrodes at 5 mA cm⁻²/2 mAh cm⁻². (e) Cycling performance of the Zn||Zn cell at 9 mA cm⁻²/4.5 mAh cm⁻² (10 μm Zn foil with a DOD of 68%, which is close to the practical application), the prolonged lifespan verifies its excellent performances in protecting Zn anodes.

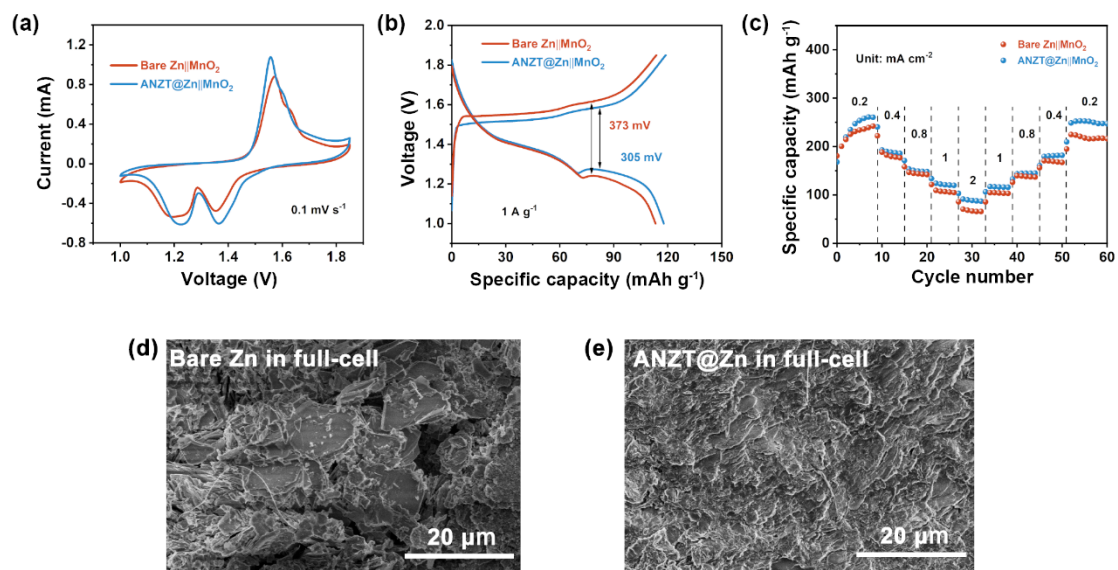


Fig. S10 (a) CV curves, (b) charge/discharge curves, and (c) rate performance of Zn||MnO₂ cell with bare Zn and ANZT@Zn anodes. SEM images of (d) bare Zn and (e) ANZT@Zn anodes after cycling in Zn||MnO₂ full-cells for 500 cycles (at 1 A g⁻¹).

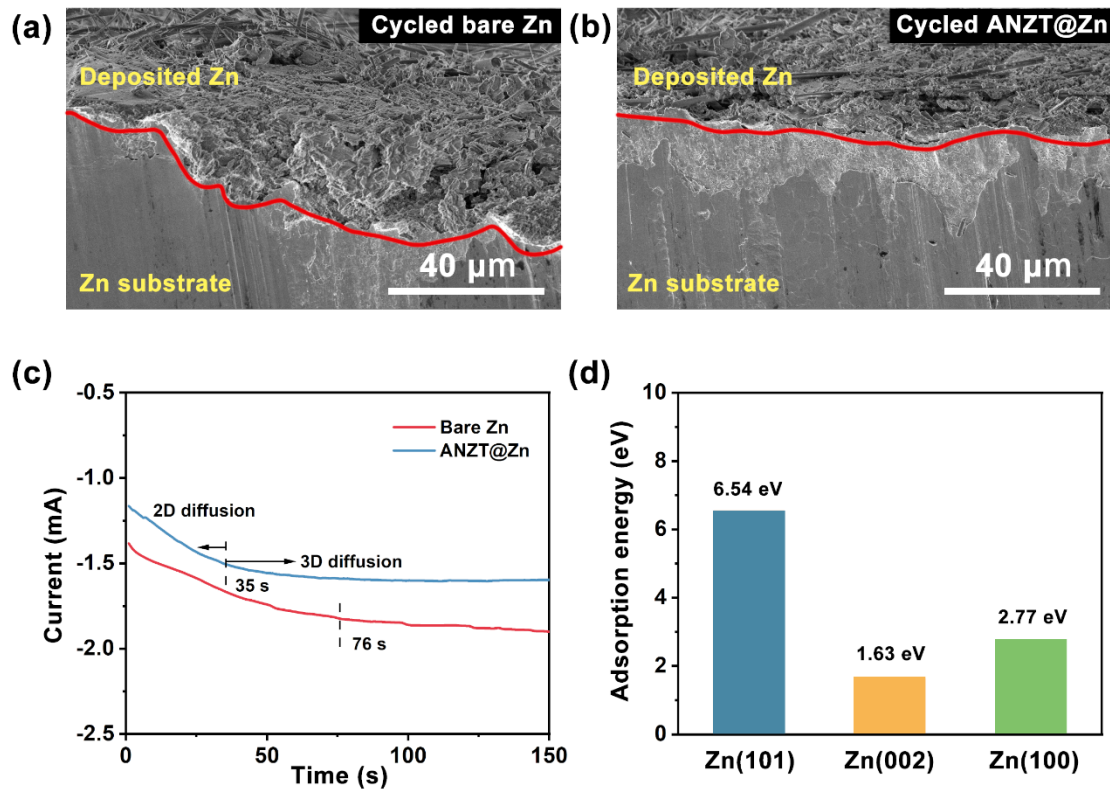


Fig. S11 The side-view SEM images of (a) bare Zn and (b) ANZT@Zn anodes after cycled in symmetric cells for 50 cycles ($5\ \text{mAh cm}^{-2}/2.5\ \text{mAh cm}^{-2}$). (c) Chronoamperometry result of symmetric cells with bare Zn and ANZT@Zn anodes under a constant overpotential of $-100\ \text{mV}$. (d) Calculated adsorption energy of Zn(101), Zn(002), and Zn(100) planes toward the TeO_3^{2-} group.

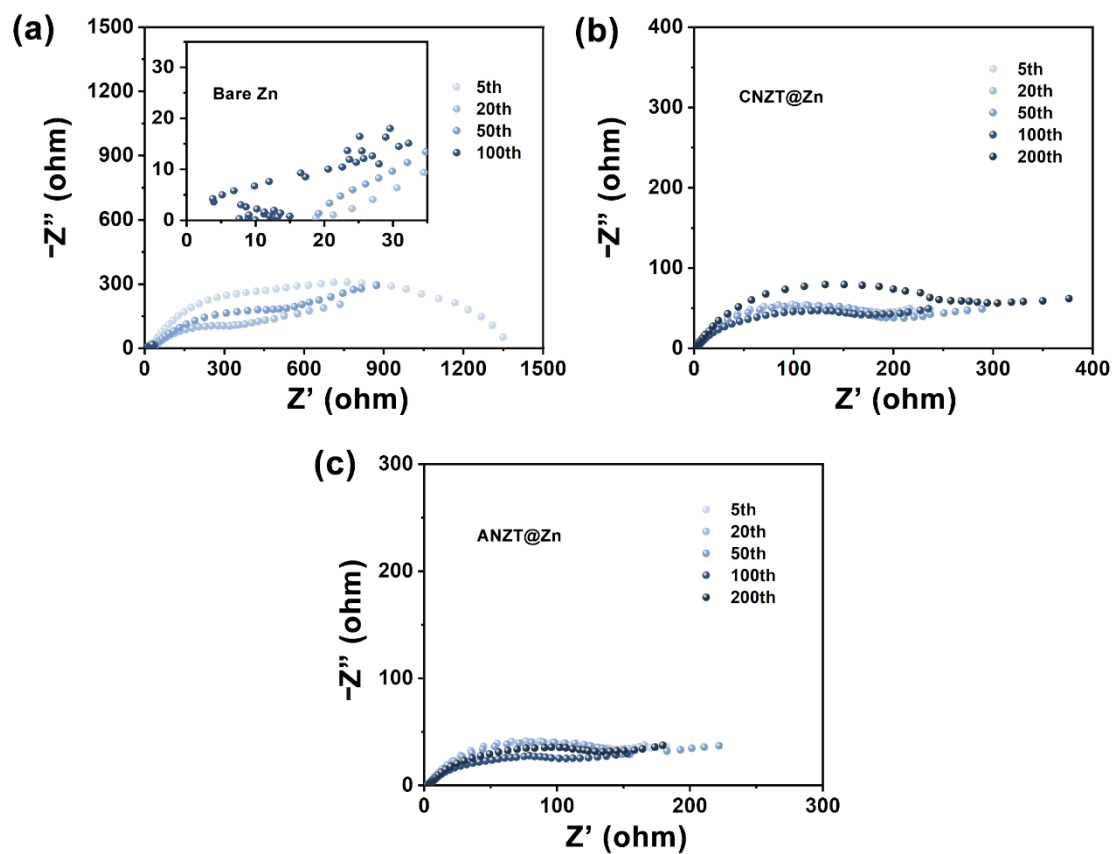


Fig. S12 Nyquist plots of symmetric cells with different Zn anodes after different cycles (at $5 \text{ mA cm}^{-2}/2.5 \text{ mAh cm}^{-2}$).

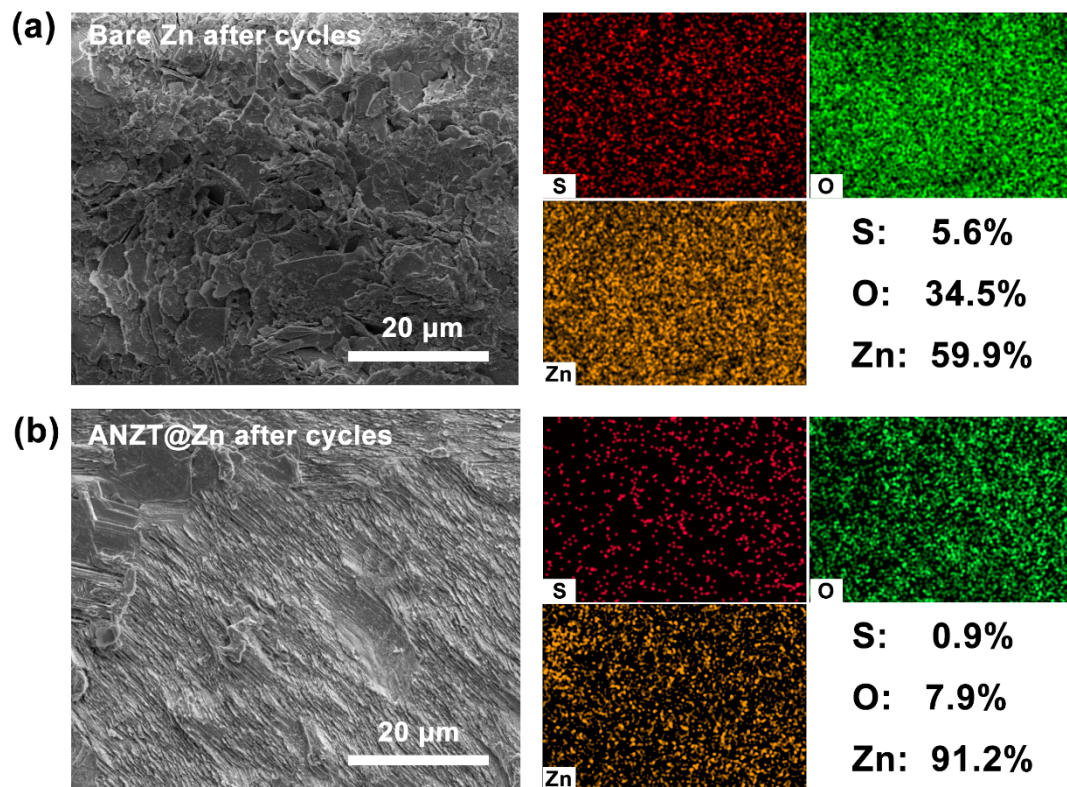


Fig. S13 SEM images of (a) bare Zn and (b) ANZT@Zn anodes after cycled in symmetric cells for 50 cycles at $5 \text{ mA cm}^{-2}/2.5 \text{ mAh cm}^{-2}$ with corresponding EDS mapping results.

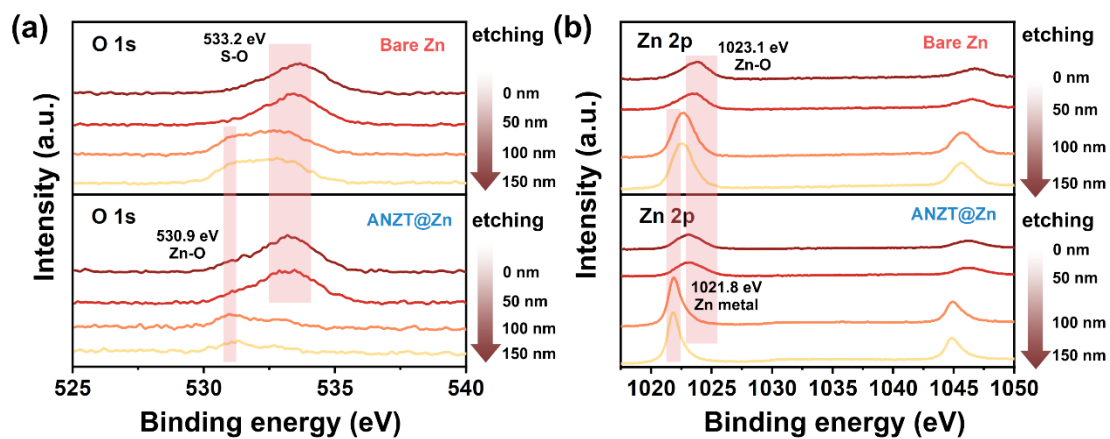


Fig. S14 High-resolution XPS spectra of (a) O 1s and (b) Zn 2p of cycled bare Zn and ANZT@Zn anodes (after 50 cycles in the symmetric cells at $5 \text{ mA cm}^{-2}/2.5 \text{ mAh cm}^{-2}$) after Ar^+ -etching for 0 nm, 50 nm, 100 nm, and 150 nm.

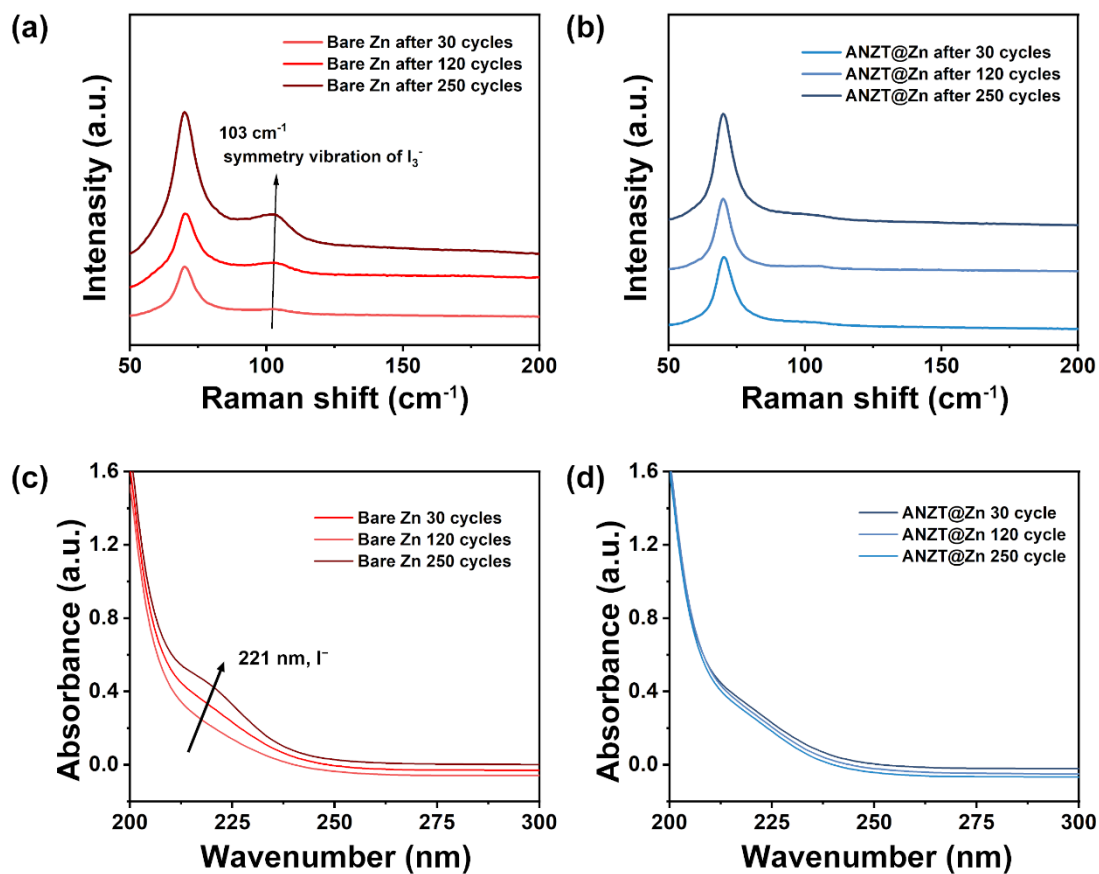


Fig. S15 (a,b) Raman and (c,d) UV-Vis spectra of bare Zn and ANZT@Zn anodes after cycling in $\text{Zn}||\text{I}_2$ cells for 10, 30, 120, and 250 cycles at 1 A g^{-1} .

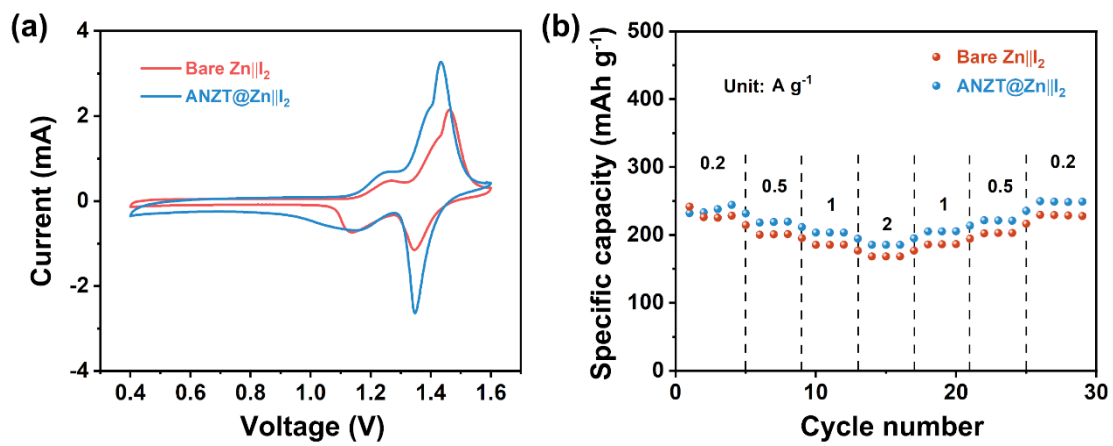


Fig. S16 (a) CV curves measured at 1 mV s⁻¹, and (b) rate performance of Zn||I₂ cells with bare Zn and ANZT@Zn anodes.

Table S1. The ICP measured Na, Zn, and Te elements contents in the CNZT and ANZT samples.

Sample	Element	Sample mass (g)	Constant volume (mL)	Content of element (mg kg ⁻¹)	Average content of element (mg kg ⁻¹)	Content of element (%)
CNZT	Na	0.05	25	833.236	830.79	0.08%
				827.09		
				832.045		
ANZT	Na	0.05	25	828.372	830.721	0.08%
				832.052		
				831.738		
CNZT	Zn	0.05	25	292566.319	292280.521	29.25%
				292914.433		
				291360.81		
ANZT	Zn	0.05	25	292697.285	293118.289	29.31%
				295233.412		
				291424.169		
CNZT	Te	0.05	25	520336.056	519343.21	51.93%
				521268.991		
				516424.583		
ANZT	Te	0.05	25	518594.968	518545.217	51.85%
				517199.311		
				519841.372		

Table S2. Performance comparison of dendrite-free Zn anode strategies between this work and other reported studies.

Materials	Areal Current (mA cm ⁻²)	Areal Capacity (mAh cm ⁻²)	Lifespan (h)	Ref.
ANZT	1	1	2760	This work
	20	5	800	
PVDF@Sn	5	55	500	[3]
SALs	1	0.5	2500	[4]
	1	1	1200	
Zn(OR) ₂	1	1	1250	[5]
	10	5	450	
Ni@NiO@Ag	10	1	250	[6]
Zn(002)	22	2	520	[7]
CIL	5	2	720	[8]
CCI	1	1	1100	[9]
	10	1	880	
ESM	5	5	450	[10]

Table S3. Performance comparison of high cathode loading pouch cells between this work and other reported studies.

Cathode materials	Mass loading (mg cm ⁻²)	Current density	Cycle number and capacity retention	Ref.
I ₂ /C	9.75	1 A g ⁻¹	600, 92.7%	This work
I ₂ /C	6.20	1C	100, 68%	[11]
VO ₂	5.84	1 A g ⁻¹	330, 60%	[12]
LiMn ₂ O ₄	7.20	1C	500, 62%	[13]
I ₂ /C	2.10	2 A g ⁻¹	350, 80%	[14]
I ₂ /C	7.35	2 A g ⁻¹	100, 64%	[15]
I ₂ /C	16.40	1 A g ⁻¹	200, 72%	[16]
NaV ₃ O ₈	10.00	0.5 A g ⁻¹	300, 84.7%	[17]
LiMn ₂ O ₄	3.00	1C	300, 84%	[18]

Reference

- [1] H. Pan, Y. Shao, P. Yan, Y. Cheng, K. Han, Z. Nie, C. Wang, J. Yang, X. Li, P. Bhattacharya, K. T. Mueller, J. Liu, *Nat. Energy* **2016**, *1*, 16039.
- [2] F. Cui, D. Wang, F. Hu, X. Yu, C. Guan, G. Song, F. Xu, K. Zhu, *Energy Storage Mater.* **2022**, *44*, 197-205.
- [3] Q. Cao, Y. Gao, J. Pu, X. Zhao, Y. Wang, J. Chen, C. Guan, *Nat. Commun.* **2023**, *14*, 641.
- [4] Z. Wei, S. Wang, D. Li, S. Yang, S. Guo, G. Qu, Y. Yang, H. Li, *Energy Environ. Sci.* **2024**, *17*, 5440.
- [5] T. Li, S. Hu, C. Wang, D. Wang, M. Xu, C. Chang, X. Xu, C. Han, *Angew. Chem. Int. Ed.* **2023**, *62*, e202314883.
- [6] Y. Gao, Q. Cao, J. Pu, X. Zhao, G. Fu, J. Chen, Y. Wang, C. Guan, *Adv. Mater.* **2023**, *35*, 2207573.
- [7] J. Zhang, W. Huang, L. Li, C. Chang, K. Yang, L. Gao, X. Pu, *Adv. Mater.* **2023**, *35*, 2300073.
- [8] Z. Zheng, D. Ren, Y. Li, F. Kang, X. Li, X. Peng, L. Dong, *Adv. Funct. Mater.* **2024**, *34*, 2312855.
- [9] H. Tian, J. Yang, Y. Deng, W. Tang, R. Liu, C. Xu, P. Han, H. Fan, *Adv. Energy Mater.* **2023**, *13*, 2202603.
- [10] W. Guo, L. Xu, Y. Su, Z. Tian, C. Qiao, Y. Zou, Z. Chen, X. Yang, T. Cheng, J. Sun, *ACS Nano* **2023**, *18*, 10642–10652.
- [11] J. Ma, A. Azizi, E. Zhang, H. Zhang, A. Pan, Ke Lu, *Chem. Sci.* **2024**, *15*, 4581.
- [12] Q. Zhang, J. Liang, M. Li, J. Qin, Y. Zhao, L. Ren, W. Liu, C. Yang, X. Sun, *Chem. Eng. J.* **2023**, *474*, 145981.
- [13] Y. Zhang, Y. Zhang, J. Deng, R. Xue, S. Yang, Y. Ma, Z. Wang, *Adv. Funct. Mater.* **2024**, *34*, 2310995.
- [14] Z. Wen, Z. Hu, X. Wang, Y. Zhang, W. Du, M. Ye, Y. Tang, X. Liu, C. Li, *Adv. Mater.* **2024**, *36*, 2407390.
- [15] Z. Hu, X. Wang, W. Du, Z. Zhang, Y. Tang, M. Ye, Y. Zhang, X. Liu, Z. Wen, C. Li, *ACS Nano* **2023**, *17*, 23207–23219.
- [16] W. Li, K. Wang, K. Jiang, *J. Mater. Chem. A* **2020**, *8*, 3785.
- [17] Y. Zhang, Z. Liu, X. Li, L. Fan, Y. Shuai, N. Zhang, *Adv. Energy Mater.* **2023**, *13*, 2302126.
- [18] J. Zhou, F. Wu, Y. Mei, Y. Hao, L. Li, M. Xie, R. Chen, *Adv. Mater.* **2022**, *34*, 2200782.